ROYAL SOCIETY OF CHEMISTRY

PAPER

Check for updates

Quantifying polycrystallinity effects on skyrmion dynamics and device performance

Ahmet Bahadır Trabzon, [ID] †[ab] Arash Mousavi Cheghabouri [ID] †[c] and
Mehmet Cengiz Onbaşlı [ID] *[cd]

Skyrmion-based devices promise energy-efficient spintronic functionalities, but polycrystalline magnetic films can degrade performance by inducing skyrmion pinning. Here, we use micromagnetic modeling to quantify the impact of polycrystallinity-induced variability in key material parameters such as saturation magnetization, Dzyaloshinskii–Moriya interaction, and uniaxial anisotropy on skyrmion stability, dynamics, and hysteresis loops in Co/Pt films and device geometries. We demonstrate that variations exceeding 5% in these parameters across grains significantly increase the likelihood of pinning, with the effects depending on both grain size and distribution. Our findings establish quantitative tolerance thresholds and highlight the importance of fabricating films with narrow grain size distributions and stringent control over material uniformity to enable robust, pinning-free operation in skyrmion-based spintronic devices.

1. Introduction

Spintronic devices that harness topological magnetic structures such as skyrmions hold great promise for energy-efficient computing, memory, and logic applications.[1–4] However, their transition from fundamental research to practical technologies is impeded by material inhomogeneities—most notably, the effects of polycrystallinity in thin films.[5] Grain boundaries introduce local variations in magnetic properties, leading to skyrmion pinning that disrupts motion and induces stochastic device behavior.[6,7] Although several experimental studies have observed these effects,[8–10] a comprehensive theoretical and numerical framework to quantify the impact of polycrystallinity on skyrmion dynamics remains lacking. This gap limits the ability to design reliable and reproducible skyrmion-based devices.

Skyrmion pinning sites arise from local variations in magnetic parameters and the polycrystalline nature of magnetic interfaces. Overcoming these pinning sites typically requires higher current densities, which in turn lead to significant Joule heating and thermal drift. To mitigate these effects, experimental demonstrations have relied on pulsed current operation with low duty cycles and low-temperature conditions.[11] While such approaches have enabled proof-of-concept results, polycrystallinity and the resulting

inhomogeneities continue to limit device functionality and reliability.

To address these challenges, we developed micromagnetic models to systematically quantify the impact of polycrystallinity on skyrmion motion and device performance. Using Voronoi-based polycrystalline geometries, we introduced statistical variations in key magnetic parameters, saturation magnetization, Dzyaloshinskii–Moriya interaction, and uniaxial anisotropy, to realistically capture material inhomogeneities. We evaluated how grain size distributions and parameter fluctuations influence skyrmion pinning, stability, and transport. This approach enables the identification of critical tolerance thresholds for material uniformity, offering practical design guidelines for skyrmion-based devices with reduced susceptibility to pinning-related defects.

Previous studies have explored the influence of polycrystallinity on spintronic devices, but many relied on simplified models that did not capture realistic distributions of material parameters.[12–14] Several approaches assumed uniform or periodically varying anisotropies,[15] overlooking the discrete nature of grains in nanoscale devices. Similarly, earlier experimental efforts to mitigate pinning lacked systematic insights into how grain-dependent magnetic properties affect device reliability.[16,17] Our work addresses this gap by providing a quantitative framework that captures the stochastic nature of polycrystalline materials, enabling predictive design strategies for skyrmion-based technologies.

The remainder of this paper is structured as follows. We first describe the methodology used to model polycrystallinity in micromagnetic simulations. This is followed by our results on skyrmion dynamics and pinning effects, which we compare with previous theoretical and experimental studies. Finally, we

a Department of Electrical and Electronics Engineering, Boğaziçi University, Bebek, Istanbul 34342, Turkey
b Department of Physics, Boğaziçi University, Bebek, Istanbul 34342, Turkey
c Department of Electrical and Electronics Engineering, Koç University, Sariyer, Istanbul 34450, Turkey. E-mail: monbasli@ku.edu.tr
d Department of Physics, Koç University, Sariyer, Istanbul 34450, Turkey
† These authors contributed equally to this work

discuss the key findings and conclude with design considerations for improving skyrmion-based device performance.

2. Methods

To analyze the effects of material parameter variability, particularly in M_{sat}, K_u, and D_{ind}, across polycrystalline Voronoi regions, we performed micromagnetic simulations of hysteresis loops, anisotropy, and skyrmion dynamics in racetrack and logic gate geometries.[2,3] We also investigated how the number of Voronoi regions affects both hysteresis behavior and skyrmion motion.

2.1. Micromagnetics

Our simulations were performed using MuMax3 software,[18] which implements the finite-difference method to solve the Landau–Lifshitz–Gilbert (LLG) equation. Each magnetization vector has a magnitude corresponding to the saturation magnetization M_{sat}. In the presence of exchange stiffness (A_{ex}), uniaxial anisotropy (K_u), and Dzyaloshinskii–Moriya interaction (DMI) (D_{ind}), spins tend to align with an effective field given by

$$\vec{H}_{eff} = -\frac{1}{\mu_0 M_{sat}} \frac{\delta \mathscr{E}_{tot}}{\delta \vec{m}}$$ (1)

where the total energy density $\mathscr{E}_{tot}$ is the sum of contributions from exchange, Zeeman, demagnetization, anisotropy, and DMI energies:

$$\begin{aligned} \mathscr{E}_{tot} &= A_{ex}(\nabla\vec{m})^2 - \mu_0 M_{sat}\left(\vec{m}\cdot\vec{H}_{ext}\right) \\ &\quad - \mu_0 M_{sat}\left(\vec{m}\cdot\vec{H}_{demag}\right) - K_u(\vec{m}\cdot\hat{z})^2 \\ &\quad + D_{ind}[m_z\nabla\cdot\vec{m} - (\vec{m}\cdot\nabla)m_z] \end{aligned}$$ (2)

here, $\vec{H}_{ext}$ and $\vec{H}_{demag}$ denote external and demagnetizing fields, respectively. All simulations assume the uniaxial anisotropy axis is oriented along the out-of-plane $\hat{z}$-direction.

We focus on both hysteresis loops and skyrmion dynamics. For hysteresis simulations, the system is relaxed for each external magnetic field step until equilibrium is reached. In

contrast, skyrmion dynamics require solving time-dependent equations using the LLG equation with spin-transfer torque:

$$\frac{d\vec{m}}{dt} = -\frac{\mu_0\gamma}{1+\alpha^2}\left\{\vec{m}\times\vec{H}_{eff} + \alpha\left[\vec{m}\times\left(\vec{m}\times\vec{H}_{eff}\right)\right]\right\}$$ (3)

where γ is the gyromagnetic ratio and α is the damping constant. We use two spin-transfer torque terms to manipulate skyrmions: Slonczewski-type spin-transfer torque (STT) for current-perpendicular-to-plane (CPP) geometries and Zhang-Li STT for current-in-plane (CIP) configurations. In the CIP model, the Zhang-Li torque is defined as:

$$\vec{\tau}_{ZL} = \frac{1}{1+\alpha^2}\left\{(1+\xi\alpha)\vec{m}\times[\vec{m}\times(\vec{u}\cdot\nabla)\vec{m} + (\xi-\alpha)\vec{m}\times(\vec{u}\cdot\nabla)\vec{m}]\right\}$$ (4)

where

$$\vec{u} = \frac{\mu_B\mu_0}{2e\gamma_0 B_{sat}(1+\xi^2)}\vec{j}.$$ (5)

where ξ is the non-adiabaticity parameter, $\gamma_0 = \gamma\mu_0$, μ_0 is the vacuum permeability, μ_B is the Bohr magneton, e electron charge, B_{sat} saturation field, and $\vec{j} = j\hat{x}$ is CIP. To eliminate skyrmion Hall effect, we used $\xi = \alpha$ which simplifies $\vec{\tau}_{ZL}$ to

$$\vec{\tau}_{ZL} = \frac{1}{1+\alpha^2}\frac{\mu_B\mu_0 j}{2e\gamma_0 B_{sat}}\vec{m}\times\left(\vec{m}\times\frac{\partial\vec{m}}{\partial x}\right).$$ (6)

2.2. Modeling multi-crystallinity

We modeled polycrystalline structures using Voronoi tessellations, which emulate the grain morphology found in thin magnetic films. A custom Python script was developed to generate Voronoi patterns within a given simulation domain. Seed points were randomly distributed in the x–y plane to create distinct Voronoi regions, each representing a single crystallite. Formally, for a set of seed points p_i, $i = 0,1,\ldots,N$, the corresponding Voronoi cell V_i is defined such that:

$$V_i = \left\{(x,y)\in\mathbb{R}^2 : ||(x,y) - p_i|| \le ||(x,y) - p_j|| \forall i \ne j\right\}$$ (7)

Each Voronoi region was assigned local magnetic properties drawn from normal distributions centered around nominal values of M_s, K_u, and D_{ind} with the investigated standard deviations. These variations mimic the physical inhomogeneities introduced by polycrystallinity in real materials. For simple geometries such as rectangles or racetracks, the Voronoi tessellation was applied across the full simulation domain. For more complex device layouts (e.g., skyrmion logic inverters), the tessellation was masked using the device outline to restrict the polycrystalline regions to the active magnetic area (Fig. 1).

2.3. Simulation and statistical techniques

For each simulation configuration, we generated multiple random realizations of polycrystalline structures to capture the statistical variability introduced by grain-dependent material fluctuations. Each realization included a unique Voronoi tessellation and a random sampling of local values for M_{sat}, K_u,

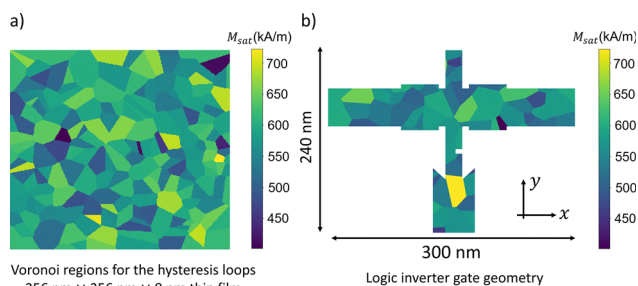**Fig. 1** Demonstration of Voronoi regions on (a) 256 nm × 256 nm × 8 nm thin film and (b) logic inverter gate.[2,3]

This journal is © the Owner Societies 2025

Phys. Chem. Chem. Phys., 2025, **27**, 19694–19702 | **19695**

and D_{ind} drawn from normal distributions centered around nominal values with specified standard deviations (*e.g.*, $\sigma = 1\%$, $\sigma = 3\%$, $\sigma = 5\%$, $\sigma = 7\%$).

For hysteresis loop simulations, the grid size was set to $256 \times 256 \times 1$, with cell sizes of 1 nm $\times$ 1 nm $\times$ 8 nm. Material parameters within each Voronoi region followed a normal distribution with a standard deviation of $\sigma = 10\%$.

For each simulation, distributions of the key parameters were independently generated across the Voronoi tessellation. We analyzed both in-plane and out-of-plane hysteresis behavior. At each field step, the system was allowed to relax until convergence was reached. Field increments were taken in steps of 0.5% of the saturation field B_{sat}, where B_{sat} is defined as the external field strength required to fully align the magnetization. For skyrmion dynamics, we used both mean values and distributions of material parameters. Simulations were repeated for a large number of statistical realizations to extract both average behavior and stochastic deviations. Unless stated otherwise, $A_{ex} = 15$ pJ m^{-1} was used for all simulations. For simulations of skyrmion dynamics, mean values of $M_{sat} = 580$ kA m^{-1}, $K_u = 0.8$ MJ m^{-3}, $D_{ind} = 3.5$ mJ m^{-3} were used.

3. Results

3.1. Hysteresis loop comparisons

We set the Dzyaloshinskii–Moriya interaction constant to $D_{ind} = 0.4$ mJ m^{-2}, the uniaxial anisotropy constant to $K_u = 1$ kJ m^{-3}, and varied the mean saturation magnetization M_{sat} throughout the thin film. Fig. 2 shows the grain distribution and corresponding values of M_{sat}. The same grain geometry was reused for other parameter sweeps to ensure consistent comparisons.

We fixed $M_{sat} = 400$ kA m^{-1} and varied the film thickness from 1 nm to 8 nm to examine how multi-crystallinity influences the in-plane hysteresis loops. The coercive field B_c was found to vary with both the number of Voronoi regions and the film thickness. As shown in Fig. 3a, the influence of multi-crystallinity becomes more pronounced in thicker films, where the difference in B_c between multi-crystalline and single-crystalline films increases. For an 8 nm film, we swept through various values of M_{sat}, and the corresponding hysteresis loops are presented in Fig. 3b. The coercive field B_c increases linearly with M_{sat} for 50 and 250 regions, ranging from 0 to 10 mT. In contrast, for other region counts, the dependence is non-linear, and B_c is typically between 20–30 mT, which is significantly higher than in the 50 and 250 region cases.

Out-of-plane hysteresis simulations revealed magnetic vortex patterns at certain film thicknesses. The vortex cores were primarily dictated by the underlying multi-crystalline region distributions. Representative examples are shown in Fig. 4. Notably, while vortex patterns are typically absent in single-crystalline films at greater thicknesses, they did emerge in some multi-crystalline configurations.

To study the effect of anisotropy variations, we varied K_u across Voronoi regions while fixing $M_{sat} = 580$ kA m^{-1}. K_u values ranged from -10^5 and 10^5 J m^{-3}. The effective anisotropy, defined as $K_{eff} = K_u - \frac{1}{2}\mu_0 M_{sat}^2$, differs by less than 5% for both positive and negative K_u when K_u is less than 10^4 J m^{-3} due to $\frac{1}{2}\mu_0 M_{sat}^2 = 4.2 \times 10^5$ J m$^{-3} \gg 10^4$ J m^{-3} being much larger than K_u. As a result, low K_u values have similar effects regardless of sign.

Polycrystallinity significantly reduced the coercive fields in in-plane hysteresis loops compared to single-crystalline structures. This reduction was most pronounced in the 100-region configuration across all tested K_u values except for $K_u = 10^5$ J m^{-3}, where the 250-region case showed the largest reduction (see Fig. S4). Additionally, the slope of the out-of-plane hysteresis loops increased with higher K_u values.

Finally, we fixed $M_{sat} = 580$ kA m^{-1} and $K_u = 1$ kJ m^{-3}, and evaluated five different region counts along with the single-crystalline case by introducing spatial variation in D_{ind}. We did not sweep across D_{ind} values, as it significantly affects the saturation field B_{max}. Instead, we compared three cases:

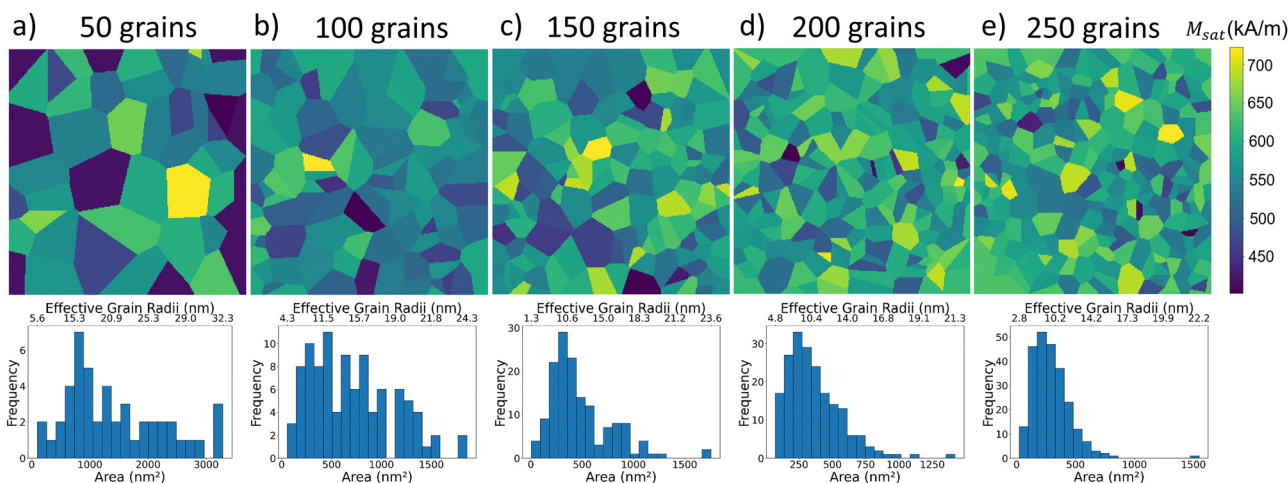**Fig. 2** Illustration of grain size distributions for (a) 50, (b) 100, (c) 150, (d) 200, (e) 250 grains on 256 nm $\times$ 256 nm $\times$ 8 nm thin film.

19696 | *Phys. Chem. Chem. Phys.*, 2025, **27**, 19694–19702
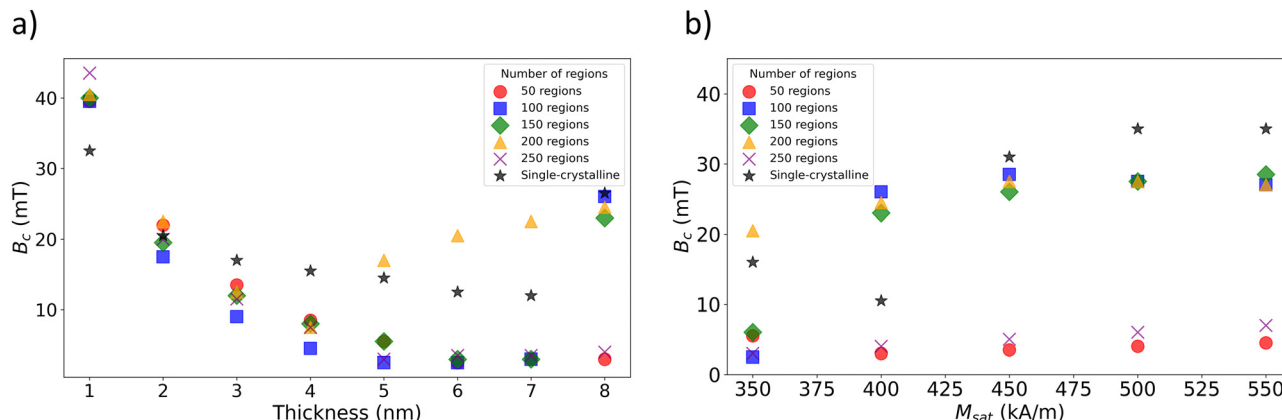
This journal is © the Owner Societies 2025

Fig. 3 (a) Coercive fields *versus* thickness of the film for 5 different numbers of regions and single-crystalline case when M_{sat} = 400 kA m^{-1}. Effects of multi-crystallinity becomes significant for thicker films. (b) Coercive fields *versus* M_{sat} for the film thickness of 8 nm where the effects of multi-crystallinity is more visible.
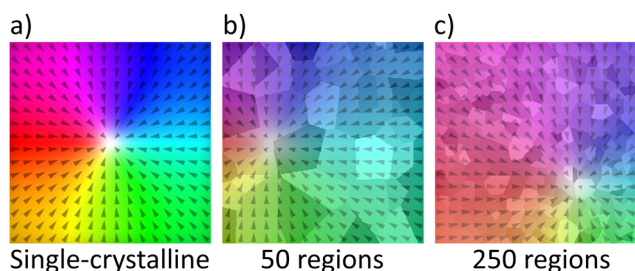

Fig. 4 Example vortex profiles on 256 nm × 256 nm × 8 nm: (a) single-crystalline (b) number of regions: 50 (c) number of regions: 250. Depending on the number of regions, vortex profiles may or may not occur. Locations of vortex centers change depending on the distribution of regions.

$D_{ind} = \pm 0.4$ mJ m^{-2}, and $D_{ind} = 0$ mJ m^{-2}. In the 8 nm films, introducing polycrystallinity led to a 5–10% increase in the in-plane coercive field across both D_{ind} cases. The corresponding hysteresis loops are shown in Fig. S6.

3.2. Skyrmion dynamics in skyrmion racetracks

We simulated a polycrystalline racetrack with dimensions of 50 nm × 250 nm, in which material parameters varied spatially across the structure. The parameter variations were modeled as Gaussian distributions with specified means and standard deviations.

In the top row of Fig. 5d, skyrmion dynamics are simulated within a 50 nm × 250 nm slab is divided into 100 parts, resulting in an effective radius of approximately 6.31 nm per part. The motion of the skyrmion is tracked under varying material parameters. Under these conditions, after 8.0×10^{11} A m^{-2} no pinning is observed for the simulated parameters. In the bottom row of Fig. 5d, the slab is divided into 70 segments. Here, we observe a threshold (cutoff) current density for simulations involving variations in Dzyaloshinskii–Moriya interaction and uniaxial anisotropy. However, no cutoff was observed when only the saturation magnetization was varied.

In real polycrystalline materials, the exchange interaction across grain boundaries is often reduced. To capture this effect,

we divided the 50 nm × 250 nm polycrystal film into approximately 100 segments and decreased the exchange interaction between grains by 10%. Skyrmions were driven using a current density of $j = 5 \times 10^{11}$ A m^{-2} for 4 ns. As in earlier simulations, we introduced variations in each material parameter independently, with standard deviations of $\sigma = 2\%$ and $\sigma = 4\%$.

For each case, we performed 30 simulation runs and calculated the skyrmion pinning probability. These results are compared with simulations that did not include reduced exchange at grain boundaries. Table 1 summarizes the pinning probabilities within 4 ns. A slight increase in pinning probability is observed when the exchange interaction is reduced, especially for higher disorder levels.

3.3. Skyrmion dynamics in skyrmionic logic gates

The multi-crystallinity of materials affects the performance of skyrmionic devices. We investigated the effects of multi-crystallinity on Boolean-universal skyrmionic logic gates proposed in ref. 3, in which any type of logic operation can be obtained by combining fundamental blocks.

We specifically analyzed the inverter gate, as its logic function can be realized with a single block. The device operates in three stages: initialization, transmission/blocking, and clearance. Fig. 6 summarizes the working principle of the device.

$0 \rightarrow 1$ Operation: Skyrmions are driven in the device from left to right by the Zhang-Li spin transfer torque (STT). When there is no skyrmion at the bottom of the device the input is 0, and the right-probing skyrmion moves to the right end of the device, resulting in an output of 1.

We investigated the effects of variations in material parameters (M_{sat}, K_u, D_{ind}) across Voronoi regions on the device performance. We swept through the standard deviation values σ of the normally distributed material parameters for 5 different region counts on the base image: 50, 100, 150, 200, 250 which correspond to average grain radii of 21.4 nm, 15.1 nm, 12.4 nm, 10.7 nm, and 9.57 nm, respectively. We observed that if $\sigma > 5\%$ for any parameter, success rates of the device drastically decrease for most cases. Therefore, we analyzed
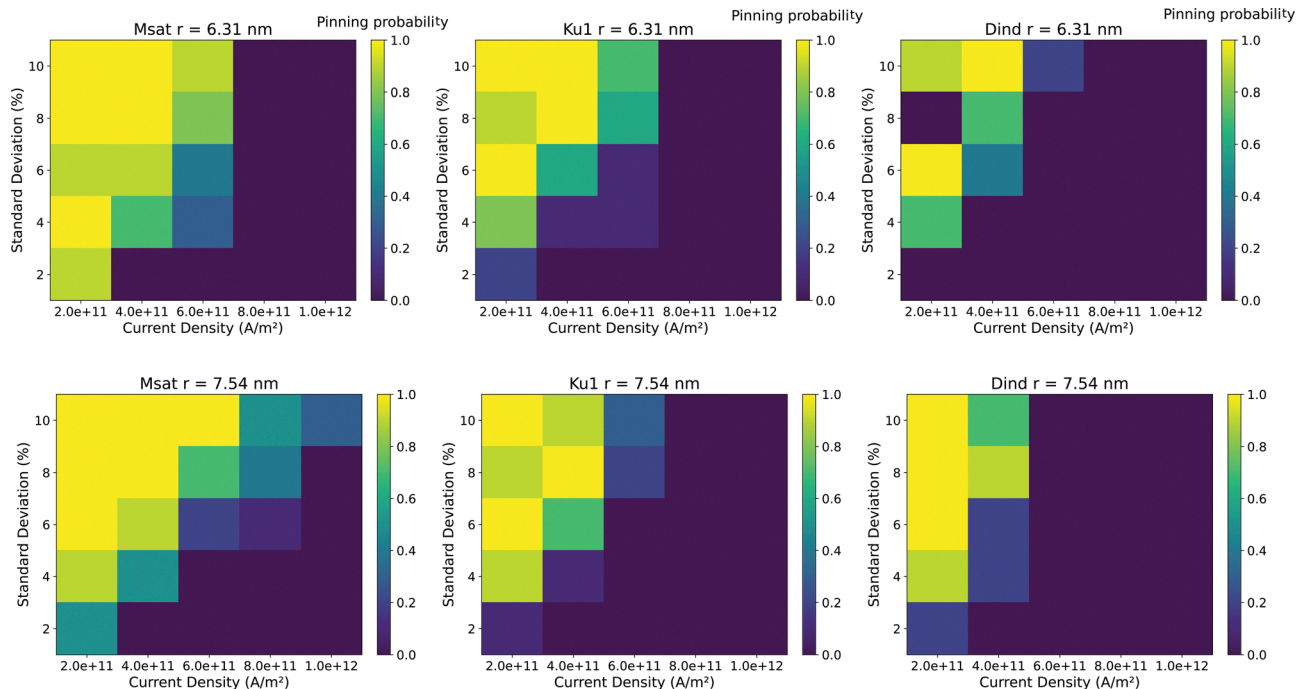
This journal is © the Owner Societies 2025

Phys. Chem. Chem. Phys., 2025, **27**, 19694–19702 | **19697**

Fig. 5 Plots for the pinning probability for a skyrmion in a racetrack for different grain sizes.

Table 1 Pinning probabilities of skyrmions within 4 ns for different parameters with and without reduction of exchange among grains

	$\sigma = 2\%$		$\sigma = 4\%$	
	Reduced exchange	Without reduction	Reduced exchange	Without reduction
M_{sat}	21/30	16/30	22/30	20/30
K_u	4/30	3/30	26/30	26/30
D_{ind}	11/30	7/30	27/30	25/30

the interval of $\sigma = 0$–4% in detail by running batch simulations for each combination of σ and region counts (Fig. 7 and 8).

Increasing the standard deviation of any parameter intensified skyrmion pinning. For each combination of number of grains and σ, we ran 50 simulations with different random seeds meaning that we ran 2000 simulations for each parameter. Success rates for each parameter is shown in Fig. 8a–c. Within the analyzed regime, average success rates of the $0 \rightarrow 1$ operation for variations on M_{sat}, K_u, and D_{ind} are 42.95%, 49.45%, and 36.95%, respectively. Increasing σ decreased the success rates. For each parameter, number of 250 regions decreased the success rates. However, there is no simple relation between number of points and success rates, success rate is parameter-dependent.

$1 \rightarrow 0$ Operation: To block the incoming skyrmion, a domain wall is created during the initialization stage. The incoming skyrmion is then blocked by the domain wall at the neck of the device, fulfilling the $1 \rightarrow 0$ condition.

We simulated $1 \rightarrow 0$ operation similar to $0 \rightarrow 1$ operation, introducing multi-crystallinity and checked whether the operation is successful or not. Success rates for each parameter are shown in Fig. 8d–f. Within the analyzed regime, average
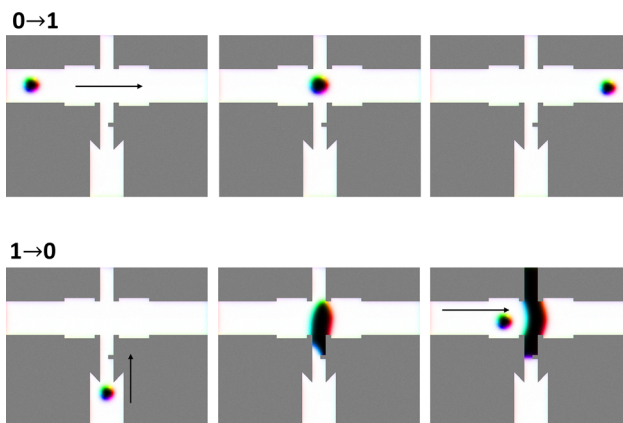

Fig. 6 The skyrmionic inverter gate performs logic operations for both the $0 \rightarrow 1$ and $1 \rightarrow 0$ transitions. A skyrmion is periodically sent from the left to the right of the device, while the input is applied from the bottom. When there is no input, the skyrmion propagates freely through the device, resulting in an output of 1. Conversely, when the input is 1, a domain wall forms at the neck of the device, blocking the periodically sent skyrmion. As a result, the output is realized as 0. Finally, in the clearance stage (not shown in the figure), a current is applied to the top of the device, removing the domain wall and skyrmion to prepare the device for the next operation.

success rates of the $1 \rightarrow 0$ operation for variations on M_{sat}, K_u, and D_{ind} are 34.33%, 33.34%, and 21.29%, respectively.

4. Discussion

4.1. Hysteresis loops and device performance

In the hysteresis loop simulations, we observed distinct magnetic profiles depending on the grain size and film thickness.
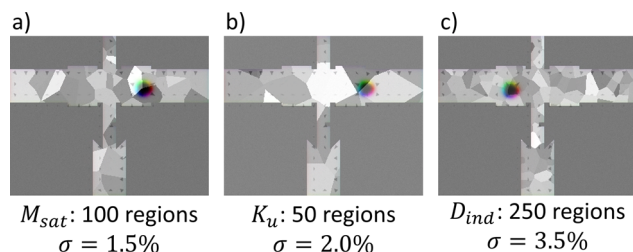
19698 | *Phys. Chem. Chem. Phys.*, 2025, **27**, 19694–19702

This journal is © the Owner Societies 2025

Fig. 7 Some examples of pinned skyrmions across Voronoi regions when introduced variations on (a) M_{sat}, (b) K_u, and (c) D_{ind}.

Increasing the film thickness made the effects of multi-crystallinity more pronounced. We attribute this behavior to the contribution of the film's out-of-plane magnetization to the demagnetizing field. The introduction of multi-crystallinity alters the magnetic energy landscape and demagnetizing fields, thereby affecting the magnetic configuration of the films. These changes in the magnetic and energy profiles can hinder skyrmionic device performance by causing skyrmion pinning. Using different grain distributions, we conducted batch simulations to evaluate the success rates of skyrmionic devices, specifically a logic inverter gate. The operation mechanisms of the logic gate differ between the $0 \rightarrow 1$ and $1 \rightarrow 0$ cases, relying on current-driven skyrmions and domain wall formation, respectively. Consequently, the success rates obtained from the simulations vary between these two cases. Since domain wall structures are generally less stable than skyrmions, their formation is significantly affected when polycrystalline materials are used.

A similarity between the two cases is that increasing the standard deviation of material parameters across Voronoi regions generally decreases the success rates. We also observed that the most sensitive parameter for overall device performance is D_{ind} in both cases. However, we did not observe any trivial relationship between the success rates and the number of Voronoi regions.

In addition to pinning behavior, a likely reason for failure is that skyrmion trajectories become distorted and their velocities fluctuate in polycrystalline regions, despite constant current injection.

4.2. Pinning from a theoretical perspective

Skyrmion radius can be expressed analytically by the following equation:[19]

$$R = \pi D_{ind} \sqrt{\frac{A_{ex}}{16 A_{ex} K_{eff}^2 - \pi^2 D_{ind}^2 K_{eff}}} \qquad (8)$$

where $K_{eff} = K_u - \frac{1}{2}\mu_0 M_{sat}^2$ is effective anisotropy constant. This analytical expression is derived by minimizing the total energy density given in eqn (2) with respect to both the skyrmion radius and wall width as independent variables.

In polycrystalline materials, deviations of parameters from their mean values across grains cause different stable skyrmion radii in each grain. Larger differences in R between regions increase the probability of pinning due to the energy cost associated with a skyrmion moving between grains that prefer different sizes. Each grain has its own optimal skyrmion radius
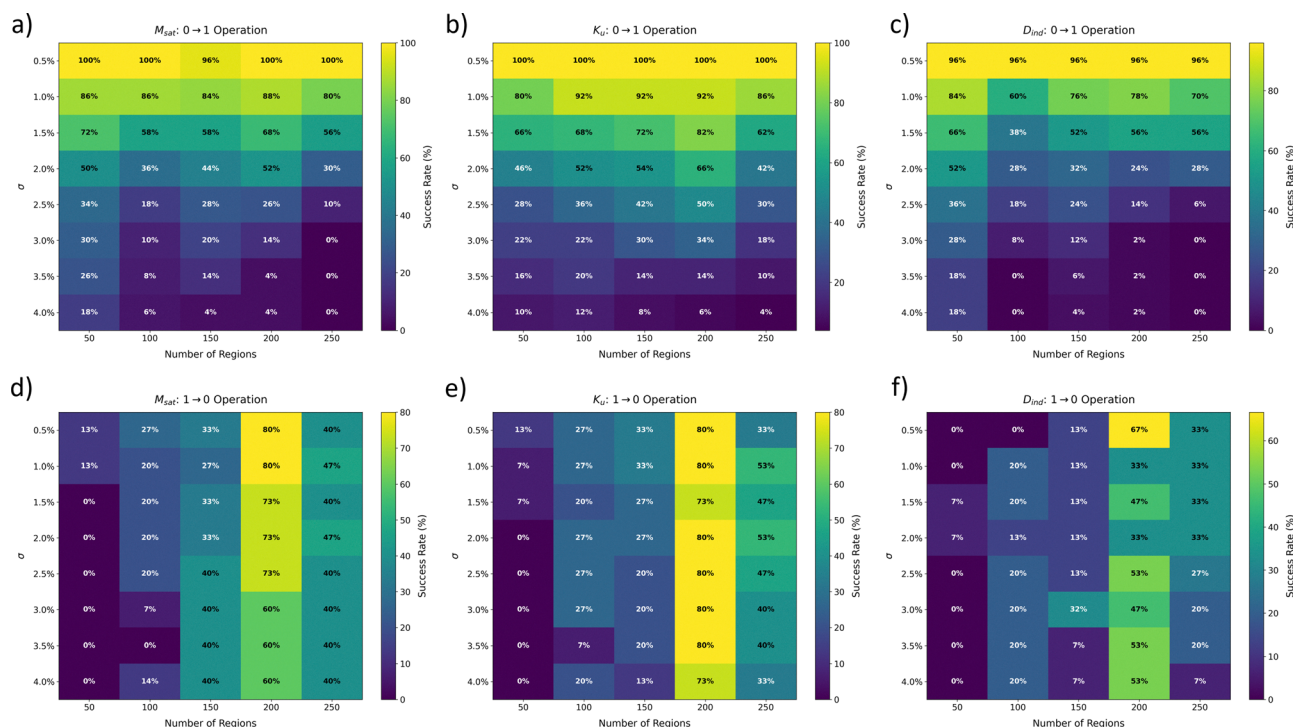

Fig. 8 Success rates of logic operations $0 \rightarrow 1$ (a)–(c) and $1 \rightarrow 0$ (d)–(f). Values lower than 100 correspond to device failures.

This journal is © the Owner Societies 2025

Phys. Chem. Chem. Phys., 2025, **27**, 19694–19702 | **19699**

based on its local material properties. When a skyrmion attempts to move from one grain to another, it must either retain its original size (which incurs an energy penalty in the new environment) or adjust its size to match the preferred radius of the new grain (which also costs energy). These energy barriers hinder skyrmion motion, creating pinning sites that trap skyrmions or require external forces to overcome. This also explains why applying higher currents lowers pinning probabilities, as shown in Fig. 5.

Taking the partial derivatives of eqn (8), fractional radius changes ($\delta R/R$) can be related to fractional changes in material parameters. Using the parameters in Section 2.3, the following relations are obtained,

$$\left(\frac{\delta R}{R}\right)_{M_{sat},K_u} = \frac{\delta D_{ind}}{D_{ind}}\left(1 - \frac{1}{\frac{16 A_{ex}K_{eff}}{\pi^2 D_{ind}^2} - 1}\right) = -4.94\frac{\delta D_{ind}}{D_{ind}} \quad (9)$$

$$\left(\frac{\delta R}{R}\right)_{M_{sat},D_{ind}} = \frac{\delta K_u}{K_u}\frac{K_u}{K_{eff}}\frac{\pi D_{ind}^2 - 32 A_{ex}K_{eff}}{32 A_{ex}K_{eff} - 2\pi D_{ind}^2} = -1.61\frac{\delta K_u}{K_u} \quad (10)$$

$$\left(\frac{\delta R}{R}\right)_{K_u,D_{ind}} = \frac{\delta M_{sat}}{M_{sat}}\left(-\mu_0\frac{M_{sat}^2}{K_{eff}}\right)\frac{\pi D_{ind}^2 - 32 A_{ex}K_{eff}}{32 A_{ex}K_{eff} - 2\pi D_{ind}^2}$$
$$= 0.853\frac{\delta M_{sat}}{M_{sat}} \quad (11)$$

From these equations, it is clear that the most sensitive parameter affecting pinning is D_{ind} which is consistent with the results shown in Fig. 8.

The above sensitivity coefficients were obtained by perturbing one parameter at a time. However, in real polycrystalline films M_{sat}, K_u, and D_{ind} may fluctuate simultaneously and with non-zero correlations. Hence, opposing K_u–M_{sat} (eqn (10) and (11)) variations can partially cancel out their net effect on R, while additive K_u–D_{ind} (eqn (9) and (10)) variations act cooperatively and amplify it, potentially enhancing pinning. This indicates that reliable device design should consider the full covariance structure of grain-to-grain parameter variations rather than independent tolerances alone.

Even though this theoretical sensitivity analysis may give insights into skyrmion pinning, it has several limitations when applied to real polycrystalline systems. The analytical expression assumes isolated skyrmions in an infinite medium and treats parameter variations as smooth continuous changes, while polycrystalline materials present a more complex environment where skyrmions interact with grain boundaries, other skyrmions, and structural defects, and experience abrupt transitions in crystal structure and magnetic properties at grain boundaries that lead to pinning mechanisms beyond simple size mismatch. Additionally, this static equilibrium approach neglects dynamic effects and current-induced torques that are important in real device operation. Despite these limitations, the sensitivity analysis provides valuable guidance for understanding which material parameters most strongly influence pinning behavior and serves as a starting point for more

sophisticated models that account for the complex microstructural environment of polycrystalline materials.

Beyond the size-based analysis above, skyrmion structure fundamentally affects pinning sensitivity.[20] For thin-wall skyrmions ($R/w \gg 1$ where w is domain wall widths of skyrmions) with distinct core and wall regions, exchange and DMI variations primarily affect the wall region, making these skyrmions highly sensitive across grains. Thick-wall skyrmions ($R/w \approx 1$) lack distinct regions and are primarily sensitive to anisotropy variations, as the entire structure responds to K_u changes. This distinction explains why parameter tolerances may differ depending on skyrmion operating conditions and applied magnetic fields that control the thin-wall to thick-wall transition.

4.3. Effects of reduced exchange among grains

In realistic polycrystalline materials, grain boundaries may act as regions with reduced exchange stiffness. This reduction in exchange stiffness increases the skyrmion pinning probability. Along grain boundaries, this reduction also causes a suppression in the transmission of torque across grains. Hence, the effective torque acting on a skyrmion when driven by spin-polarized currents is reduced especially around a grain boundaries. From a micromagnetic perspective, the Heisenberg exchange energy between neighboring spins is given by $E_{ex} = -J\vec{S}_i\cdot\vec{S}_j$, and the corresponding torque is proportional to $\tau \propto A_{ex}\vec{S}_i \times \vec{S}_j$. A decrease in exchange stiffness A_{ex} at grain boundaries reduces the interfacial exchange torque. As a result, the driving torque exerted by neighboring grains becomes insufficient to coherently propagate the skyrmion through the disordered landscape. This effect confines the skyrmion within the local energy well defined by a single grain or a cluster of grains, thereby increasing the probability of pinning. The results in Table 1 support this explanation, as pinning probabilities increase in the presence of reduced exchange stiffness near grain boundaries for all tested material parameters.

4.4. Effects of temperature

The polycrystalline effects presented in these results do not include random thermal field fluctuation effects due to finite temperatures. The random magnetic anisotropy field term originating from finite temperature noise could be included in the micromagnetic models. This term might serve to de-pin skyrmions by nudging them out of a local energy minimum, while stability of skyrmions is also reduced due to the random spatial drift effects due to local grain geometries and their demagnetization fields. Our room temperature micromagnetic models showed that skyrmion stability is significantly diminished compared to the 0 K models. Recent studies of skyrmion pinning by localized defects reveal that thermal de-pinning follows Arrhenius behavior:[20] $\tau(T) = \tau_0 e^{\Delta E/k_B T}$, where τ is lifetime of skyrmions and the activation energy ΔE depends on the pinning potential depth. Thus, even though thermal field may help de-pin skyrmions, overall device performance is hindered because of the unstable skyrmions under thermal field.

19700 | Phys. Chem. Chem. Phys., 2025, 27, 19694–19702

This journal is © the Owner Societies 2025

Our micromagnetic models might therefore underestimate the pinning probabilities and variability. In any case, a polycrystalline film structure must be designed to have low gradients in magnetic parameters in the first place to avoid failing under the further detrimental effects thermal gradient fields. Our results provide essential insights on the effects of using polycrystalline materials on spintronic device operations and their reliability. We believe that these insights might make or break the future success of low-power spintronic devices and grain engineering with uniform magnetic material parameters is essential.

4.5. Experimental concerns

In polycrystalline skyrmion systems, experimental values of critical current densities and skyrmion motion reliability vary significantly due to microstructural inhomogeneities. For instance, amorphous or polycrystalline multilayers such as $[Pt/GdFeCo/MgO]_{20}$ exhibit blurred skyrmion boundaries and require high current densities (e.g., 4.23×10^{11} A m^{-2} with 5 ns pulses) for motion, as demonstrated in STXM imaging experiments.[11] These requirements are influenced by pinning sites at grain boundaries, amorphized regions in the layers, increased damping, and Joule heating, which are not fully captured by idealized micromagnetic models. Moreover, experiments[21] have shown that longer pulse widths reduce the critical current density, but this trade-off is limited by heating effects. Thus, our reported current thresholds are model-specific and should be interpreted as illustrative trends rather than absolute values, underscoring the complexity of direct experimental-model comparisons in non-ideal systems.

Based on our findings, achieving low variability in Dzyaloshinskii–Moriya interaction (DMI) and maintaining grain sizes larger than device dimensions are critical for robust skyrmion device performance. Material systems such as Ta/CoFeB/MgO are promising due to their tunable perpendicular magnetic anisotropy and well-characterized DMI behavior, especially when fabricated with atomic-scale thickness precision. Among deposition techniques, sputtering remains the most practical for device fabrication, but key parameters such as sputtering pressure, total film thickness, substrate temperature, and post-deposition annealing conditions strongly influence grain morphology and interfacial quality. Lower sputtering pressures and moderate annealing temperatures typically yield larger grains and sharper interfaces, both of which are essential for reducing parameter fluctuations and suppressing skyrmion pinning. Thus, careful control of deposition and thermal treatment parameters is essential to meet the material uniformity thresholds we identified through micromagnetic modeling.

We identify that standard deviations in material parameters greater than 5% can significantly reduce skyrmion device reliability, but we do not present a universal guideline table, since these critical thresholds vary with film stack type, magnetic layer thickness, and device geometry. Instead, our simulations provide a framework that can be adapted to specific material systems and geometries by re-running the parameter sensitivity analyses under application-specific device geometry, stack and grain size distribution constraints.

This work presents several novel contributions that advance the understanding and design of skyrmion-based spintronic devices beyond prior studies. While the role of polycrystallinity in skyrmion pinning has been qualitatively acknowledged, we introduce a quantitative tolerance framework that defines critical fluctuation thresholds in key magnetic parameters (M_{sat}, K_u, D_{ind}) beyond which device functionality is compromised. Our use of Voronoi-based polycrystalline geometries, combined with thousands of micromagnetic simulations, enables statistically meaningful predictions of skyrmion pinning probabilities and device success rates. Furthermore, we derive analytical sensitivity relationships linking material parameter fluctuations to skyrmion radius and pinning risk, revealing DMI as the most sensitive contributor. Importantly, our findings are translated into actionable fabrication guidelines, including recommended material stacks and deposition process parameters to mitigate polycrystallinity-induced failures. These contributions represent a comprehensive and practical framework that bridges micromagnetic theory with real-world device engineering, offering insights not previously addressed in the literature.

Author contributions

A. B. T. modeled the magnetic hysteresis loops of the polycrystalline films. A. M. C. wrote the Voronoi generator code as a Python package, modeled the racetrack. Both A. B. T. and A. M. C. modeled the logic inverter gate. A. B. T. and M. C. O. wrote the initial draft. M. C. O. supervised the study. All authors read and edited the manuscript.

Conflicts of interest

The authors declare no competing interests related to this study.

Data availability

All data of the study are available from the authors or from SI. The Python package code for Voronoi generator is in the SI. The logic gate model scripts were provided in the SI of ref. 2. See DOI: **https://doi.org/10.1039/d5cp01730k**

All code can be provided upon reasonable request.

Acknowledgements

This journal is © the Owner Societies 2025

Phys. Chem. Chem. Phys., 2025, **27**, 19694–19702 | **19701**

References

1 B. Dieny, I. L. Prejbeanu, K. Garello, P. Gambardella, P. Freitas, R. Lehndorff, W. Raberg, U. Ebels, S. O. Demokritov and J. Akerman, *et al.*, *Nat. Electron.*, 2020, **3**, 446–459.

2 A. Mousavi Cheghabouri, F. Katmis and M. C. Onbasli, *Phys. Rev. B*, 2022, **105**, 054411.

3 A. Mousavi Cheghabouri, R. Yagan and M. C. Onbasli, *Adv. Theory Simul.*, 2024, 2400243.

4 R. Tomasello, E. Martinez, R. Zivieri, L. Torres, M. Carpentieri and G. Finocchio, *Sci. Rep.*, 2014, **4**, 1–7.

5 R. Gruber, J. Zázvorka, M. A. Brems, D. R. Rodrigues, T. Dohi, N. Kerber, B. Seng, M. Vafaee, K. Everschor-Sitte and P. Virnau, *et al.*, *Nat. Commun.*, 2022, **13**, 3144.

6 C. Reichhardt and C. O. Reichhardt, *Phys. Rev. B*, 2019, **99**, 104418.

7 K. Wang, Y. Zhang, V. Bheemarasetty, S. Zhou, S.-C. Ying and G. Xiao, *Nat. Commun.*, 2022, **13**, 722.

8 K. Zeissler, M. Mruczkiewicz, S. Finizio, J. Raabe, P. Shepley, A. Sadovnikov, S. Nikitov, K. Fallon, S. McFadzean and S. McVitie, *et al.*, *Sci. Rep.*, 2017, **7**, 15125.

9 R. Juge, S.-G. Je, D. D. S. Chaves, L. D. Buda-Prejbeanu, J. Peña-Garcia, J. Nath, I. M. Miron, K. G. Rana, L. Aballe and M. Foerster, *et al.*, *Phys. Rev. Appl.*, 2019, **12**, 044007.

10 I. Gross, W. Akhtar, A. Hrabec, J. Sampaio, L. Martnez, S. Chouaieb, B. Shields, P. Maletinsky, A. Thiaville and S. Rohart, *et al.*, *Phys. Rev. Mater.*, 2018, **2**, 024406.

11 S. Woo, K. M. Song, X. Zhang, M. Ezawa, Y. Zhou, X. Liu, M. Weigand, S. Finizio, J. Raabe and M.-C. Park, *et al.*, *Nat. Electron.*, 2018, **1**, 288–296.

12 A. Salimath, A. Abbout, A. Brataas and A. Manchon, *Phys. Rev. B*, 2019, **99**, 104416.

13 D. A. Garanin and E. M. Chudnovsky, *Phys. Rev. B*, 2023, **107**, 014419.

14 L. González-Gómez, J. Castell-Queralt, N. Del-Valle, A. Sanchez and C. Navau, *Phys. Rev. B*, 2019, **100**, 054440.

15 C. Reichhardt, C. J. O. Reichhardt and M. Miloševic, *Rev. Mod. Phys.*, 2022, **94**, 035005.

16 T. Hori, N. Kanazawa, K. Matsuura, H. Ishizuka, K. Fujiwara, A. Tsukazaki, M. Ichikawa, M. Kawasaki, F. Kagawa and M. Hirayama, *et al.*, *Phys. Rev. Mater.*, 2024, **8**, 044407.

17 X. Xie, L. Kong, W. Wang, D. Song and H. Du, *Phys. Rev. B*, 2024, **109**, 104405.

18 A. Vansteenkiste, J. Leliaert, M. Dvornik, M. Helsen, F. Garcia-Sanchez and B. Van Waeyenberge, *AIP Adv.*, 2014, 4.

19 X. Wang, H. Yuan and X. Wang, *Commun. Phys.*, 2018, **1**, 31.

20 X. Gong, K. Jing, J. Lu and X. Wang, *Phys. Rev. B*, 2022, **105**, 094437.

21 W. Wang, D. Song, W. Wei, P. Nan, S. Zhang, B. Ge, M. Tian, J. Zang and H. Du, *Nat. Commun.*, 2022, **13**, 1593.

19702 | *Phys. Chem. Chem. Phys.*, 2025, **27**, 19694–19702

This journal is © the Owner Societies 2025